## Numerical simulation and experimental investigation about internal and external flows

Tao Wang [a]; Guowei Yang [a]; Guojun Huang [a]; Liandi Zhou [b]
[a] LHD of Institute of Mechanics, Chinese Academy of Sciences, Beijing, People's Republic of China [b] China Ship Scientific Research Center, Wuxi, People's Republic of China

## PLEASE SCROLL DOWN FOR ARTICLE

Taylor & Francis
Taylor & Francis Group

# Numerical simulation and experimental investigation about internal and external flows†

TAO WANG‡*, GUOWEI YANG‡, GUOJUN HUANG‡ and LIANDI ZHOU¶

‡LHD of Institute of Mechanics, Chinese Academy of Sciences, Beijing 100080, People's Republic of China
¶China Ship Scientific Research Center, Wuxi 214082, People's Republic of China

In this paper, TASCflow3D is used to solve inner and outer 3D viscous incompressible turbulent flow ($R_e = 5.6 \times 10^6$) around axisymmetric body with duct. The governing equation is a RANS equation with standard $k-\varepsilon$ turbulence model. The discrete method used is a finite volume method based on the finite element approach. In this method, the description of geometry is very flexible and at the same time important conservative properties are retained. The multi-block and algebraic multi-grid techniques are used for the convergence acceleration. Agreement between experimental results and calculation is good. It indicates that this novel approach can be used to simulate complex flow such as the interaction between rotor and stator or propulsion systems containing tip clearance and cavitation.

*Keywords*: Ship engineering; Inner and outer flow; Turbulence flow; Axisymmetric body with duct; Numerical simulation

## 1. Introduction

Zhou and Zhao (1995), which deals with the whole flow field including outer and inner flows, uses an iterative method for the simulation of the interaction between the propulsion system and its main body. As shown in Zhou and Zhao (1995), a solution which meets very tight accuracy requirement has been achieved. For CFD, the present challenge is to simulate complex flow with the relative motion of local components (for example rotor and stator), tip-leakage flow and cavitation.

With the development of the numerical technique and CFD software, 3D viscous flow analysis tends to be more and more mature. It is now possible to solve accurately the complicated viscous flow field around the ship/submarine/torpedo with realistic configurations. A great deal of manpower, resource and design cycle time can be saved due to the use of commercial software.

TASCflow is mainly used for the inner flow problem such as the turbo machine. In this paper, we attempt to use this software for the simulation of integrated inner and outer flow problem. The flow field around an axisymmetric body with a duct was calculated and the numerical result agrees very well with the experiment. It indicates

that TASCflow can be used for complex flow field due to the interaction between rotor and stator, propulsion and its carrier or tip leakage flow and cavitation.

## 2. Computational method

### 2.1 Grid generation

The computing model and testing model chosen are composed of axisymmetric body (length $L$, diameter $D$) and model duct (length $l$, diameter of inlet and outlet is $d_1$ and $d_2$, respectively). The whole flow field is divided into two parts, namely an inner flow inside the duct and an outer flow outside the duct. The domain is divided into multi-blocks, as shown in figure 1. The 3D mesh is shown in figure 2, the total number of grid is determined as follows

$$\sum_{L=1}^{n} (i \times j \times k)_L = 430{,}335 \tag{1}$$

where $i$, $j$, $k$ are the node number of grids along the three directions of hexahedron of the sub-block, $L$ is a sub-block and $n$ is the number of the sub-block.

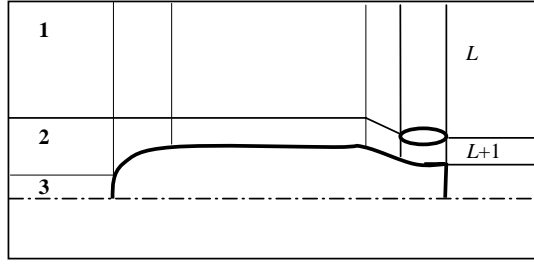*Corresponding author. Email: herot05@yahoo.com.cn

Figure 1.    Partition sketch of the flow field.

## 2.2 Governing equation

The governing equation is based on incompressible Reynolds averaged N–S equation.

### 2.2.1 Mass conservation equation

$$\frac{\partial U_j}{\partial x_j} = 0. \tag{2}$$

### 2.2.2 Momentum conservation equation

$$\frac{\partial}{\partial t}(\rho \overline{U_j}) + \frac{\partial}{\partial x}(\rho \overline{U_i U_j}) = -\frac{\partial \bar{P}}{\partial x_i} - \frac{\partial}{\partial x_j}(\overline{\tau_{ij}} + \rho \overline{u_i'' u_j''}) \tag{3}$$

where $\overline{U_i}$, $\overline{U_j}$ are averaged velocity tensors, $\rho$ is medium density,

$$\overline{\tau_{ij}} = -\mu\left(\frac{\partial U_i}{\partial x_j} + \frac{\partial U_j}{\partial x_i}\right). \tag{4}$$

## 2.3 Turbulence model

Local values of $k$ and $\varepsilon$ are obtained from the solution of the following semi-empirical transport equations

$$\frac{\partial(\rho k)}{\partial t} + \frac{\partial(\rho \overline{U_j} k)}{\partial x_j} = \frac{\partial}{\partial x_j}\left(\Gamma_k \frac{\partial k}{\partial x_j}\right) + P_k - \rho \varepsilon \tag{5}$$

$$\frac{\partial(\rho \varepsilon)}{\partial t} + \frac{\partial(\rho \bar{U}_j \varepsilon)}{\partial x_j} = \frac{\partial}{\partial x_j}\left(\Gamma_\varepsilon \frac{\partial \varepsilon}{\partial x_j}\right) + \frac{\varepsilon}{k}(c_{\varepsilon 1} P_k - \rho c_{\varepsilon 2} \varepsilon) \tag{6}$$
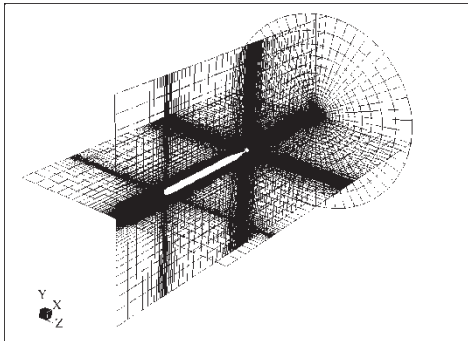


Figure 2.    The computing grids of the integrative flow field.

where the diffusion coefficients are given by the following expressions

$$\Gamma_k = \mu + \frac{\mu_t}{\sigma_k} \tag{7}$$

$$\Gamma_\varepsilon = \mu + \frac{\mu_t}{\sigma_\varepsilon}. \tag{8}$$

The production rate of turbulent kinetic energy $P_k$ is given by the expression

$$P_k = \mu_t\left(\frac{\partial \overline{U_i}}{\partial x_j} + \frac{\partial \overline{U_j}}{\partial x_i}\right)\frac{\partial \overline{U_i}}{\partial x_j}. \tag{9}$$

Therefore, the coefficient of eddy-viscosity $\mu_t$ is calculated from the product of turbulence velocity scale and turbulence length scale

$$\mu_t = \rho c_\mu \frac{k^2}{\varepsilon} \tag{10}$$

$$\rho \overline{u_i' u_j'} = \mu_t\left(\frac{\partial \bar{U}_i}{\partial x_j} + \frac{\partial \bar{U}_j}{\partial x_i}\right). \tag{11}$$

The values of all the constants in the model are given as follows

$$C_\mu = 0.09, \quad C_{\varepsilon 1} = 1.44, \quad C_{\varepsilon 2} = 1.92, \quad \sigma_k = 1.0,$$

$$\sigma_\varepsilon = 1.3.$$

## 2.4 Boundary conditions

(1)  The inlet boundary conditions are set in the front of the half length of the axisymmetric body. The conditions can be expressed as

$u = U_0$ (free stream velocity), $\quad v = 0, \quad w = 0,$

$$K_m = 3.75 \times 10^3 U_0^2, \quad \varepsilon_m = \frac{K_m^{3/2}}{0.03} \tag{12}$$

where $u$, $v$, $w$ are components of the velocity in the direction of $x$, $y$, $z$, respectively.

(2)  The outlet boundary is located at the downstream of the length of the axisymmetric body with the condition

$$\frac{\partial Q}{\partial \xi} = 0 \quad (Q = u, v, w, p, k, \varepsilon). \tag{13}$$

(3)  For the outer boundary conditions, the diameter of the computing domain is 25 times the length of the axis-symmetric body

$$\frac{\partial u}{\partial \eta} = \frac{\partial v}{\partial \eta} = \frac{\partial w}{\partial \eta} = \frac{\partial k}{\partial \eta} = \frac{\partial \varepsilon}{\partial \eta} = 0, \quad p = 0. \tag{14}$$

(4) For the wall of the axisymmetric body and duct, no slip boundary conditions are applied, that is

$$Q = 0 \, (Q = u, v, w), \quad k = 0, \quad \varepsilon = 0.$$

The near-wall region can be subdivided into three layers. In the innermost layer, the so-called "viscous sub-layer", the flow is almost laminar-like and the (molecular) viscosity plays a dominant role in momentum and heat transfer. The third layer is the region in the outer layer, called the "fully-turbulent layer", where turbulence plays a major role. Finally, there is a region between the viscous sub-layer and the fully turbulent layer, in which the wall function model is introduced due to the same importance of the molecular and turbulence viscosity.

The Reynolds number is

$$R_e = \frac{u \cdot L}{\nu} = 5.6 \times 10^6. \tag{15}$$

## 3. Numerical discretization

The mean form of governing equations can be written as a general scalar transport equation

$$\frac{\partial}{\partial t}\rho\phi + \frac{\partial}{\partial x_j}\rho u_j \phi = \frac{\partial}{\partial x_j}\left[\Gamma_{\text{eff}}\left(\frac{\partial\phi}{\partial x_j}\right)\right] + S_\phi \tag{16}$$

where $\phi$ is any parameter, such as $U_j$, $p$, $\rho$; and $S_\phi$ is a source term. Integrating equation (16) over a fixed control volume, we can get

$$\frac{\partial}{\partial t}\int_v \rho\phi\,\mathrm{d}v + \int_s \rho u_j \phi\,\mathrm{d}n_j = \int_s \Gamma_{\text{eff}}\left(\frac{\partial\phi}{\partial x_j}\right)\mathrm{d}n_j + \int_v S_\phi\,\mathrm{d}v \tag{17}$$

where $v$ and $s$ denote integral volume and integral surface, respectively, and $\mathrm{d}n_i$ represents the outward normal vector of the control surface.

How to define the control volume is a distinguishing feature of finite volume method. The computational domain is first discretized into elements. Then, control volume surfaces are defined by element mid-planes. As shown in figure 3, a control volume contains eight line-segments in two dimensions and 24 quadrilateral surfaces in three dimensions. The integral equation (17) is applied to each discrete control volume. The continuous volume integrations are converted to discrete forms, respectively. And the location of integration points for one flux element is shown in figure 4. In three dimensions, the flux element consists of eight octants and 12 integration surfaces. The surface fluxes are represented discrete form at integration points.
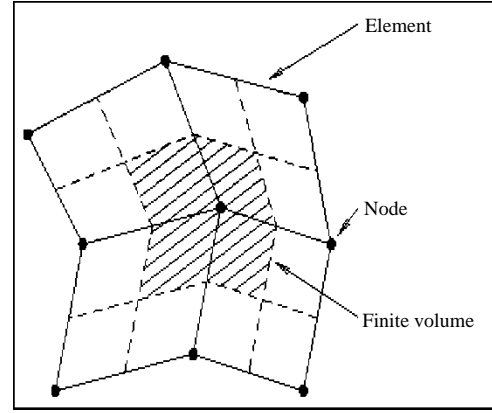


Figure 3. The definition of the control volume.

The discrete form of the integral equation is written as

$$\rho V\left(\frac{\phi - \phi^\circ}{\Delta t}\right) + \sum_{ip}\dot{m}_{ip}\phi_{ip} = \sum_{ip}\left(\Gamma_{\text{eff}}\frac{\partial\phi}{\partial x_j}\Delta n_j\right)_{ip} + \bar{S}_\phi V \tag{18}$$

where $V$ is the control volume; the subscript $ip$ represents an integration point; $\Sigma$ is the summation over all the integration points of the surface; $\Delta n_j$ represents the outward normal vector; $\Delta t$ the time step; the superscript o means the flow values at the old time level; the over-bar on the source terms indicates an averaged value of the control volume.

Several general comments:

(1) All of the velocity and surface vector are defined in Cartesian coordinates, which makes the discretization easier and is also necessary for a strongly conservative approach.
(2) The fluxes are evaluated at integration points, which can be shared by the adjacent control volume and guarantee same flux from one control volume to the next. Thus, even with a *low accuracy* advection scheme, numerical conservation is guaranteed. This is the fundamental advantage of the finite volume method.
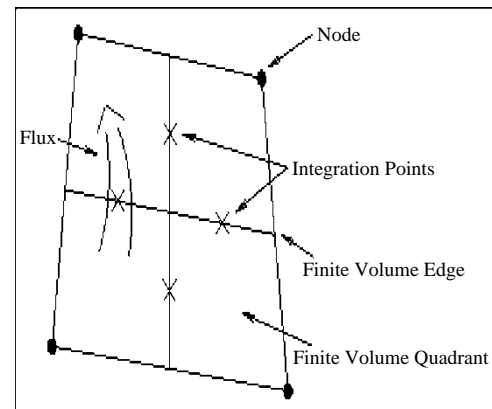


Figure 4. The definition of integration points in the 2D quadrangle element.

Table 1.   Main specifications of the HWA system in the low speed wind tunnel.

| Item | Value | Item | Value |
|---|---|---|---|
| Output voltage | $0 \sim 10\,\text{V}$ | Maximum bandwidth for probe | $250\,\text{kHz}$ |
| Equivalent input noise | $1.8\,\text{nV}/\sqrt{\text{Hz}}$ | Range of probe resistance | $2 \sim 64\,\Omega$ |
| Equivalent input drift | $0.5\,\mu\text{V}/^\circ\text{C}$ | Bridge top resistance | $20\,\Omega$ |
| Accuracy for probe resistance measurement | $0.1\% \pm 0.01\,\Omega$ | Accuracy for overheat resistor | $0.1\%$ |
| Maximum current for probe | $830\,\text{mA}$ | | |

(3) The arrangement of integration points for several abutting control volumes within one element makes discretization in multi-dimensions quite straightforward, as will be demonstrated in later sections and then the equation (18) is discretized in the respective domains.

## 4.  Linear solver

The multigrid solver used in CFX-TASCflow3D is an algebraic multigrid method (AMG) based on the additive correction multigrid (ACM) strategy. Part of the solver used in CFX-TASCflow is a multigrid method. The particular variant is based on the conservative principle, already implicitly used in the finite volume discretization and is called ACM. The solver employs the ACM strategy and is fully coupled (*i.e.* the momentum and continuity equations are solved simultaneously) and forms its blocks based on an evaluation of the coefficients of the relative strengths connecting a node to its neighbors, rather than a fixed, regular blocking. This "adaptive" approach means that the one multigrid algorithm is sufficient to reduce all the error modes in the solution, but a Block correction scheme is not required. An unstructured-grid data structure is used by the solver which allows all the connections resulting from grid-embedding, grid-attaching and periodicity to be handled fully implicitly. It also supports variable degree-of-freedom capability at each node and allows studying other future applications of full multigrid.

The solver eliminates all of the known weaknesses of the earlier multigrid algorithm and thus maintains the high level of reliability and efficiency for all the capabilities.

Multigrid methods used in AEA Technology Engineering Software Limited CFX-TASCflow (2001), which create the equations of coarse grid from the finest grid without using or knowing of the actual geometry or grid structure, have been called as "Algebraic Multigrid" (AMG) methods. Conventional multigrid methods, which are based on their blocking on the grids or on their blocking using the geometry, are termed "Geometric Multigrid", so that the two methods have different characteristics.

The relaxation scheme of an ILU solver is used. This iterative solver has the property that its solution approaches an exact 1D TDMA solution in the large coefficient direction, making it very suitable for this AMG/ACM approach. It also works well at the coupling between the velocity and pressure variables in the mass and momentum equations.

## 5.  Experiment and measurements

A physical experiment is conducted in the low speed wind tunnel in the China Ship Science Research Center (CSSRC).

### 5.1 Experimental equipment and apparatus

**5.1.1 Wind tunnel**. The low speed wind tunnel in the CSSRC is of the closed circuit type with a single return. Its closed test section is 8.5 m long with an octagonal cross section of 3.0 m in width, 3.0 m in height and 7.875 m$^2$ in area. The wind speed is continuously adjustable from 3 to 93 m/s with turbulence intensity less than 0.1% and air flow deflection less than 0.1° through the test section. The available test section size, wind speed range and air flow quality make the tunnel suitable for conventional hydrodynamic studies and developmental testing.

**5.1.2 Hot wire anemometer (HWA) system**. A set of hot wire anemometer (HWA) system (Dantec Measurement Technology Ltd 1994) of the type of stream line 90 imported from Dantec Inc. Denmark is adopted for velocity measurement. The HWA system consists of 12 constant temperature anemometer (CTA) modules, miscellaneous probes, signal conditioners and analog–digit converters. The probes used in the tests can be calibrated with an auto-calibration unit capable of the velocity range of $0.005 \sim 300$ m/s. The main specifications of the HWA system used in the CSSRC is listed in table 1.
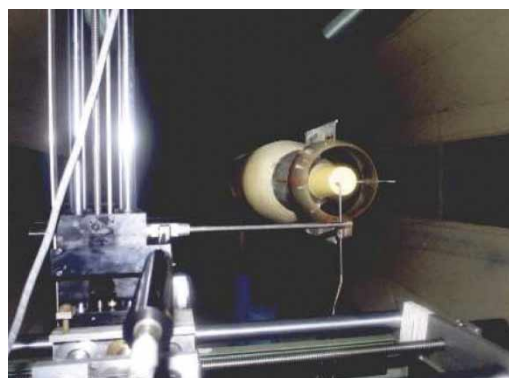


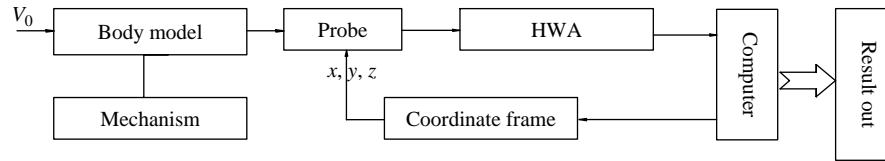Figure 5.   The photo of the experiment model and frame.

Figure 6.   The sketch of measuring system.

**5.1.3 Traversing unit**. The probe positioning is realized with the 2D traversing unit, a mechanism consisting of leading screws, stepping motors, position transducers and a controller interfaced with the HWA system. The positioning range is 600 mm in width and 1200 mm in height and the positioning accuracy is 0.1 mm. A base frame where the traversing unit is installed can also move forward and backward with the range of 500 mm, thus, the overall traversing is three-dimensional and enlarged.

**5.1.4 Mechanism for varying drift angle**. The motor-driven rotating platform of a mechanical balance works as the mechanism for varying drift angle $\beta$, with accuracy 0.1°.

**5.1.5 Host computer**. The probe positioning and velocity measurement are automatically controlled with a computer working with the HWA system.

### 5.2 Experimental method

**5.2.1 Model installation**. The model is supported within the test section by two struts with windshields around the lower half parts. The strut bases are mounted on the mechanical balance below the tunnel floor while the top ends of the struts are connected to a gimbal inside the model to align the model and change its angle of attitude. The angle of attack and roll $\alpha$ and $\varphi$ are fixed at 0° throughout the experiment while the angle of drift $\beta$ is varied with the rotating platform of the mechanical balance. When $\beta$ is equal to 0°, the model is exactly aligned to the tunnel centerline (figure 5).

**5.2.2 Probe control**. The probe is controlled with the traversing unit. When the angle of drift $\beta$ is changed, the support of the probe is correspondingly adjusted to ensure the probe always being in parallel with the model in axial direction.

**5.2.3 Wind speed**. The wind speed should be set to a considerable value to make sure the measurements performed under the condition of fully developed turbulent flow; moreover, the vibrations of the model and the probe should be taken into account. As a compromise, the wind speed is determined as $U_0 = 20$ m/s and the corresponding Reynolds number based on the characteristic length of the model is $R_e \approx 5.6 \times 10^6$.

**5.2.4 Velocity measurements**. Controlled with the host PC, the velocity measurements are automatically performed in accordance with a preset procedure. Figure 6 demonstrates the sketch of measuring system for velocity measurements.

Prior to the test program, the probes are calibrated, the probe positioning is examined and the measurements are tried. During the following test program, the velocity measurements are conducted point by point in a forward order in the axial direction and in an outward order in the radial direction respectively.

### 5.3 Test runs

As shown in table 2, the experiment is divided into 7 test runs according to the angle of drift $\beta$ and the circumferential angle $\theta$.

For each test run, 5 stations are set in the axial direction along the model centerline for the measurement point allocation. From rear to front, the 5 stations are at $x = 165$, 92.67, 25, $-80$ and $-160$ mm, respectively, but the first station ($x = 165$ mm) is behind the duct. The measurement points for the stations in the radial direction amounted to 15.6, 15.9 and 10, respectively, and for the outermost points, the radial positions are the same, i.e. $r_{\max} = 200$ mm.

The coordinate system introduced to the experiment is illustrated in figure 7 and the allocation for the measurement points in the axial and radial directions is demonstrated in figure 8.

## 6. Results and analysis

The part results of calculation and experiment are shown in figures 9–17, comparisons of the predicted results with the experimental results in the axial velocity and velocity vector are shown in figures 9 and 10, figures 11(b) and 12(b), average error is less than 5%.

Table 2.   Test runs.

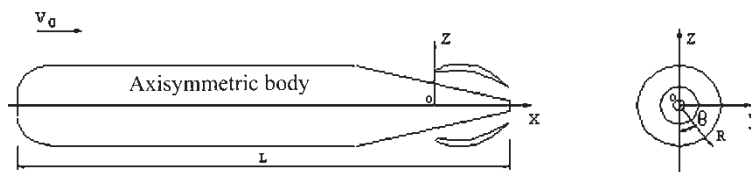| Test runs | $\theta(°)$ | $\beta(°)$ |
|---|---|---|
| $T_1$ | 0 | 0 |
| $T_2$ | 0 | $-3$ |
| $T_3$ | 0 | $-6$ |
| $S_2$ | 270 | 3 |
| $S_3$ | 270 | 6 |
| $S_4$ | 270 | $-3$ |
| $S_5$ | 270 | $-6$ |

Figure 7.   The sketch of the test coordinate.

Figures 11(a) and 12(a) show that the velocity is increasing with the diameter adding from inner to outer inside the duct; and the velocity boundary layer along the center body is thicker than that along the inner wall of the duct. And this result is concerned with the flow direction, the collocation of the duct and the taper of the body tail. The duct is located in the boundary layer as shown in figure 15 and the average velocity level in the duct is lower than that of free stream in the front of body in figures 9 and 10, but the average velocity near the duct outside seems higher than that in the front of the duct in figures 14 and 15, so the pressure level outside duct is lower and

cavitation is easier to be produced when advancing with the high speed.

Figures 13 and 16 show that pressure level inside the duct is higher than that along the central section of the body and this result is helpful to restrain the vacuole noise. Figure 17 shows that three pressure extremum points appear from head to tail, the lowest pressure in the duct suck surface is equivalent to that along the middle part of the body. But as a whole, the lowest pressure is at the body-end ($x/l = 1$) and the highest pressure at the head ($x/l = 0$).

By comparing the inner velocity field with that of the outer, it is shown that the inner and outer flow field has many differences as well as connections between them. When the flow goes up to the maximum velocity, the pressure raises up rapidly. One reason is that the line type the of the tail is shrunk along the meridian direction and the other reason is the throttle effect of the duct and small space, that is, the viscous boundary layer inside the duct decreases the flow velocity ulteriorly and meanwhile increases the pressure. In figures 13 and 15, the flow separation is produced in the end of the duct because of the difference between the outer and inner velocity/pressure and strong momentum exchanges are made among fluid molecules in different velocity. The distribution of turbulence kinetic energy illustrates that turbulence kinetic energy is maximal in the lowest pressure area. As the velocity is the lowest near the center axial line at back of the axisymmetric body and velocity is increasing with the diameter increasing, the turbulence kinetic energy near the axial line is larger and so is the turbulence intensity. However, the inner and outer flow field will be
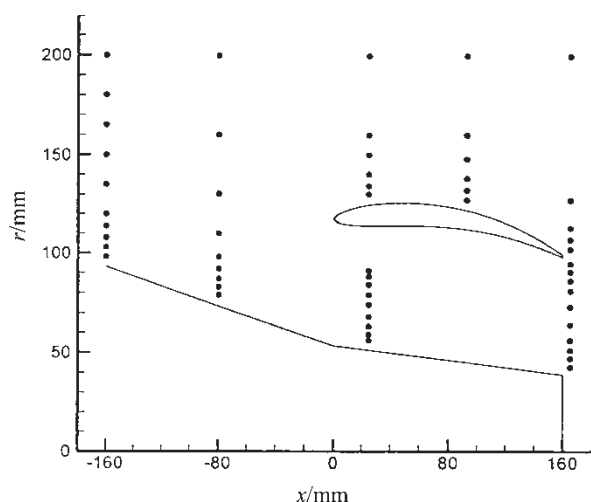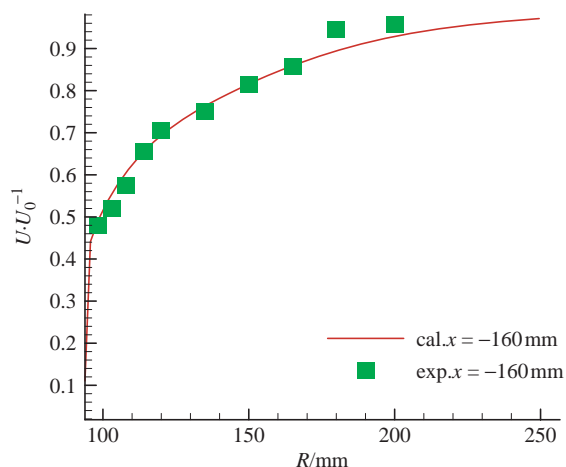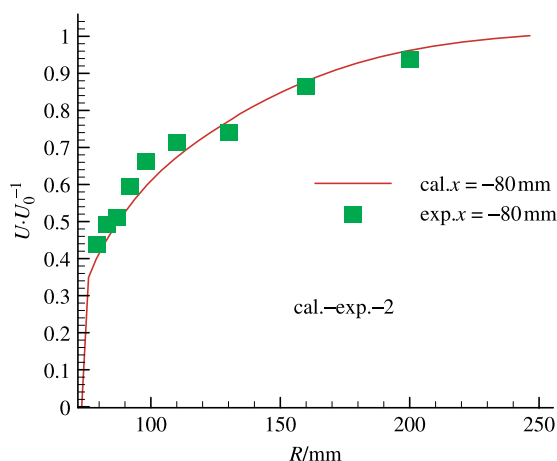


Figure 8.   The sketch of measuring points arrangement.



Figure 9.   The calculation value and experiment value of the axial velocity (average error 2.7%) for the first station $x = -160$ mm.



Figure 10.   The calculation value and experiment value of the axial velocity (average error 3.32%) for the second station $x = -80$ mm.
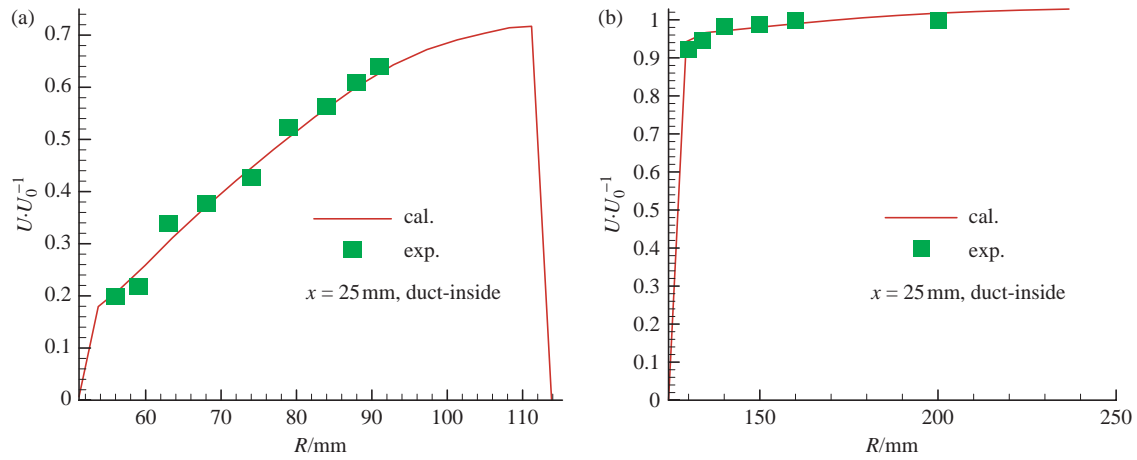
Figure 11. The calculation and experiment value of the axial velocity for the third station $x = 25$ mm. (a) Inside the duct (average error 4.11%). (b) Outside the duct (average error 3.10%).
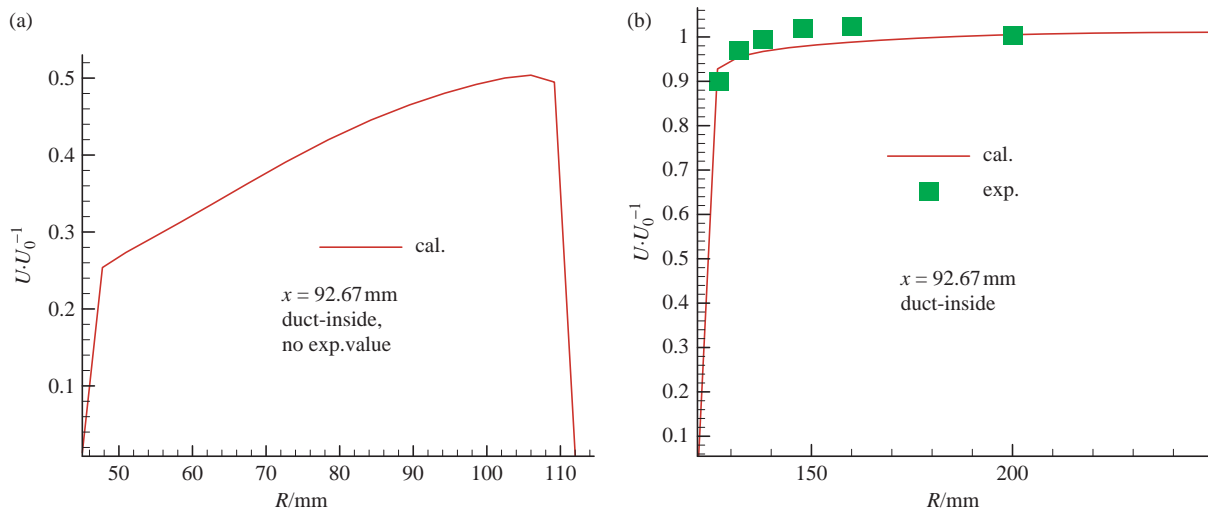


Figure 12. The calculation value and experiment value of the axial velocity for the fourth station $x = 92.67$ mm. (a) Inside the duct (no experiment value). (b) Outside the duct (average error: 2.14%).
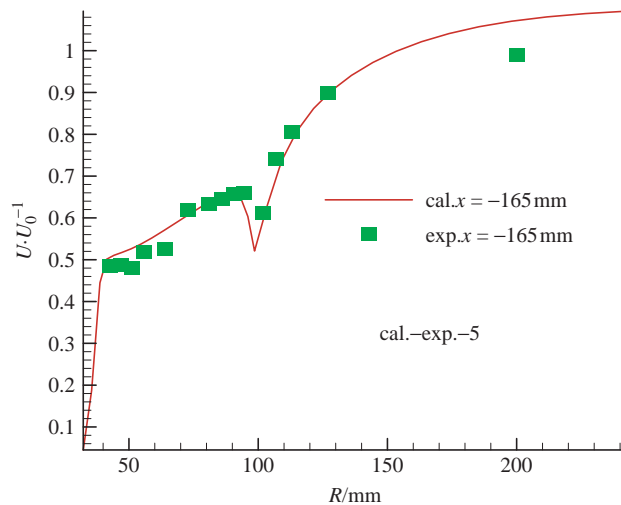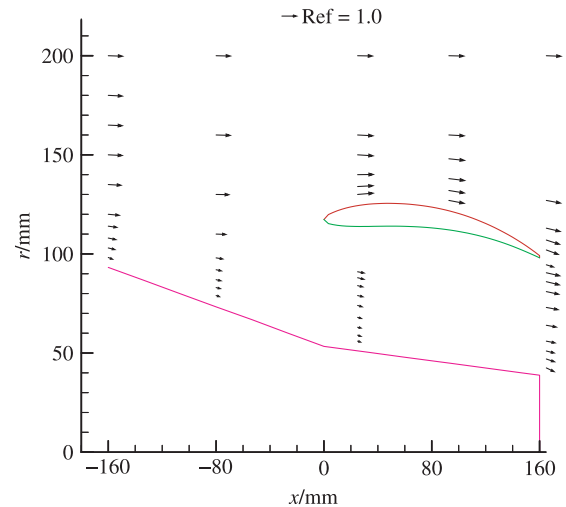


Figure 13. The calculation value and experiment value of the axial velocity (average error: 4.22%) for the fourth station $x = 165$ mm.

Figure 14. The testing velocity vector in the meridian direction ($\theta = 0°$, $\beta = 0°$).

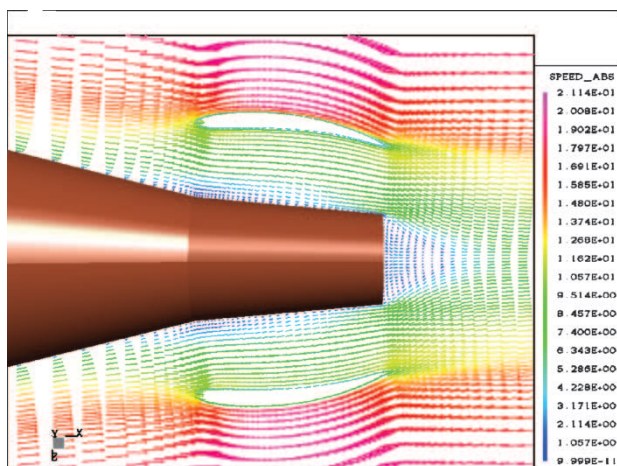Figure 15. The vector distribution of $U_{cal}$ near the tail of the axisymmetric body ($\theta = 0°$, $\beta = 0°$).



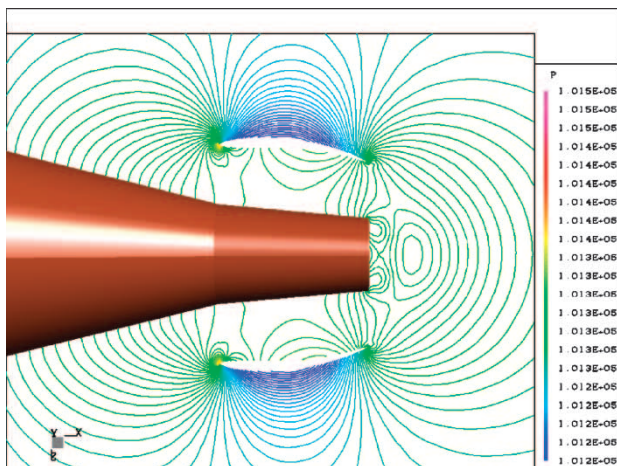Figure 17. The surface pressure distribution along the body.



Figure 16. The contour of pressure near the tail of the axisymmetric body.

mixed and tends to be uniform through momentum exchange.

## 7. Conclusion

(1) By comparing the numerical result $U_{cal}$ with the experimental result $U_{exp}$, it is shown that the average error is less than 5%, which means that TASCflow is effective for calculating the problem of inner and outer flow. The inlet boundary is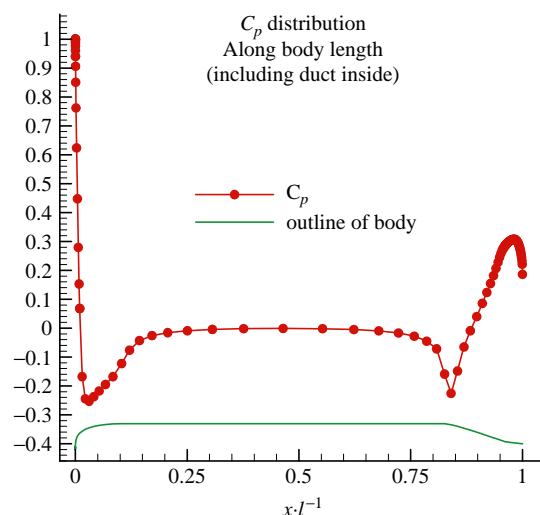 set up in the front of the half-length of the axisymmetric body and its boundary condition is free stream. The domain partition method used is more efficient and reasonable than the method given by Zhou and Zhao (1995). (2) The distribution of $U_{cal}$ shows that the thickness of the boundary layer changes with the exterior form changing along the axisymmetric body. (3) The distribution of $p$ and $U_{cal}$ shows that the resistance due to pressure difference between the head and tail-end can be decreased by changing the line type of the body.

## Acknowledgements

## References

AEA Technology Engineering Software Limited CFX-TASCflow. on help. 2001.
Dantec Measurement Technology Ltd, *StreamLine User's Guide[Z]*, 1994.
Zhou, L. and Zhao, F., An integrated method for computing the internal and external viscous flow field around the ducted propulsor behind an axisymmetric body. *Journal of Hydrodynamics, Ser. B*, 1995, **3**, 72–83.